PHOTONICS Research

67 GHz light-trapping-structure germanium photodetector supporting 240 Gb/s PAM-4 transmission

Daigao Chen,[1,2,†] Hongguang Zhang,[1,†] Min Liu,[1] Xiao Hu,[1,2] Yuguang Zhang,[1,2] Dingyi Wu,[1] Peiqi Zhou,[1] Siyao Chang,[1] Lei Wang,[1,2,3] and Xi Xiao[1,2,3,*]

[1]National Information Optoelectronics Innovation Center, China Information and Communication Technologies Group Corporation (CICT), Wuhan 430074, China
[2]State Key Laboratory of Optical Communication Technologies and Networks, China Information and Communication Technologies Group Corporation (CICT), Wuhan 430074, China
[3]Peng Cheng Laboratory, Shenzhen 518055, China
*Corresponding author: xxiao@wri.com.cn

A light-trapping-structure vertical Ge photodetector (PD) is demonstrated. In the scheme, a 3 μm radius Ge mesa is fabricated to constrain the optical signal in the circular absorption area. Benefiting from the light-trapping structure, the trade-off between bandwidth and responsivity can be relaxed, and high opto-electrical bandwidth and high responsivity are achieved simultaneously. The measured 3 dB bandwidth of the proposed PD is around 67 GHz, and the responsivity is around 1.05 A/W at wavelengths between 1520 and 1560 nm. At 1580 nm, the responsivity is still over 0.78 A/W. A low dark current of 6.4 nA is also achieved at –2 V bias voltage. Based on this PD, a clear eye diagram of 100 GBaud four-level pulse amplitude modulation (PAM-4) is obtained. With the aid of digital signal processing, 240 Gb/s PAM-4 signal back-to-back transmission is achieved with a bit error ratio of 1.6×10^{-2}. After 1 km and 2 km fiber transmission, the highest bit rates are 230 and 220 Gb/s, respectively.   © 2022 Chinese Laser Press

https://doi.org/10.1364/PRJ.455291

1. INTRODUCTION

With the rapid growth of worldwide data transmission requirements, high-speed, low-cost, and small-sized optical interconnection has made great progress in the last decades. Owing to the compatibility with commercial complementary metal–oxide–semiconductor (CMOS) processes, silicon photonics (SiP) has the advantages of large-scale monolithic integration, small footprint, and low cost [1–3], which enables it to be one of the most promising technologies for optical interconnection. Various high-performance SiP devices, including passive and active devices, have been reported in several works [4–11], which also indicates that SiP chips occupy an important place in the high-speed optical communication industry.

A photodetector (PD) is one of the crucial devices of SiP technology. Due to the indirect bandgap, silicon has low absorption efficiency at C- and O-bands. Thus, it usually grows germanium (Ge) to fabricate PD in a SiP circuit [12–14]. There are two basal structures of Ge waveguide PDs: lateral PIN [9,10,15–22] and vertical PIN [11,21–32]. All of these PDs have been reported with high opto-electrical (OE) bandwidths. For lateral PIN PD, IHP developed a 265 GHz lateral

Ge PD fabricated by a special process with highly accurate alignment of lithography and precise adjustment of critical dimensions [9]. In 2016, a 67 GHz lateral PIN Ge PD was fabricated by IMEC's SiP platform [10]. Based on this PD, a 100 Gb/s on–off keying (OOK) return-to-zero (RZ) signal was detected. For a vertical PIN PD, over 60 GHz bandwidth is reported in Refs. [11,23,24]. In Ref. [11], a Ge PD with a lateral silicon nitride input waveguide is demonstrated to support 150 Gb/s four-level pulse amplitude modulation (PAM-4) signal detection with 1 mA photocurrent.

Generally, the shape of the Ge absorption region is rectangular for both lateral and vertical PIN PDs. Optical signal is input from one side of the rectangle, and unabsorbed signal is output from the opposite side. The absorption coefficient of Ge decreases at longer wavelengths and rolls off rapidly around 1600 nm [33,34]. To improve responsivity, especially at longer wavelengths, generally it needs to lengthen the rectangular Ge absorption region. However, increasing the length means increasing parasitic parameters, i.e., capacitance [30], which will degrade the bandwidth. That is to say, there is a trade-off between the responsivity and bandwidth of a Ge PD with a rectangular absorption region. Some works employ reflection

structures in the device to increase the responsivity and shorten the length [31,32].

In this work, we propose a novel light-trapping-structure Ge waveguide PD to realize high OE bandwidth and high responsivity simultaneously. At −2 V bias, the bandwidth of the PD is about 67 GHz, and the responsivity is about 1.05 A/W at wavelengths between 1520 and 1560 nm. At 1580 nm, the responsivity can still be over 0.78 A/W. The PD also shows a low dark current, i.e., about 6.4 nA at −2 V bias. Based on the proposed PD, a clear eye diagram of a 100 GBaud PAM-4 signal is measured; 240 Gb/s PAM-4 transmission is experimentally demonstrated with a back-to-back (BTB) bit error ratio (BER) of 1.6×10^{-2}, which is under the soft decision forward error correction (SD-FEC) threshold. Offline digital signal processing (DSP) is employed to compensate for the insufficient bandwidth of the transmission system. After 1 km and 2 km single mode fiber transmission, the highest data rates reduce to 230 and 220 Gb/s, respectively, due to chromatic dispersion (CD). BTB BER versus different received optical powers with a data rate of 200 Gb/s is measured, and the receiver sensitivity is −2.5 dBm.

2. DEVICE DESIGN

There are two typical light-trapping structures: photonic crystal and circular. For photonic crystal structure, such as a grating, Ge is difficult to fabricate. In this work, we choose the circular light-trapping structure. The schematic of the proposed vertical-PIN Ge PD is shown in Fig. 1. It is fabricated on a commercial standard silicon-on-insulator (SOI) wafer with a 3 μm thick box layer and a 220 nm thick top silicon layer. The input Si waveguide is a rib waveguide, and the etching depth of the Si layer is about 130 nm; 500 nm thick Ge is selectively grown on the unetched Si area. The top of Ge is N-doped, and the silicon under Ge is P-doped.

As shown in Fig. 1, the Ge absorption area and unetched Si under Ge are circular. The silicon input waveguide is tangent to the silicon circle. Based on the boundary condition for an electromagnetic field, when the incident angle is larger than the critical angle, the input light will be totally reflected. Thus, if the radius of the circle is large enough, and the incident angle is appropriate, the light will be trapped in the light-trapping region and propagate along the edge of the circle. Then the Ge absorption region can be reused during light propagation, and the carriers will be generated until the trapped light is completely absorbed. As a result, with the same volume, the circular structure can increase the responsivity of the PD.
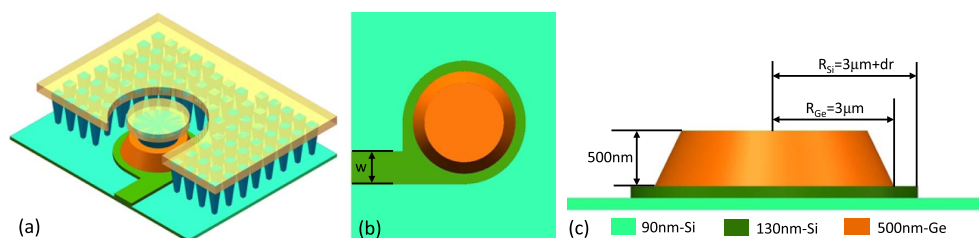
The improvement in responsivity is more effective at longer wavelengths, since the absorption coefficient at longer wavelengths is lower than that at shorter wavelengths. Due to the responsivity improvement of the light-trapping structure, the size of the absorption region can be small. The parasitic parameters, such as the capacitance of the PN junction, can also be small. Thus, compared with rectangular PDs, which use long absorption regions to increase responsivity, the proposed PD can get a better RF bandwidth without sacrificing responsivity.

The proposed PD is modeled and simulated by Ansys Lumerical FDTD Solutions. In the simulation, the absorption coefficient of Ge is set to 5000 cm^{-1} at 1550 nm, and six power monitors are used to detect the leaked light. These six power monitors form a closed cuboid, and the Ge PD is surrounded by the cuboid. Thus, all leaked light can be detected, and all un-leaked light is assumed to be absorbed by Ge. In designing of the device, we first simulate the responsivity by sweeping the radius of Ge (R_{Ge}) from 4 to 2 μm with steps of 0.5 μm. When R_{Ge} decreases from 3 to 2.5 μm, the simulated responsivity drops sharply due to the bend loss increasing dramatically, especially at longer wavelengths. So, R_{Ge} is set to 3 μm. The radius of the Si (R_{si}) circle is set to 3 μm + dr, and the width of the input waveguide is set to w. dr affects the bend loss of Si and the coupling efficiency between Si and Ge. A smaller dr will cause larger bend loss, while a larger dr will cause lower coupling efficiency between Si and Ge. Lower coupling efficiency means a longer light path in Si mesa, which also increases the bend loss of Si. w affects mode excitation in the PD. Since there are abrupt interfaces in the circular PD (e.g., between the input waveguide and silicon mesa, and between the silicon mesa and Ge mesa), an appropriate w could get the minimum bend loss induced by mode excitation. Those two parameters are optimized to improve responsivity. The figure of merit (FOM) of the optimization is defined as the sum of leaked power detected by the six power monitors. The target of optimization is to reduce the FOM to a value as small as possible. To save simulation time, we remove the metal contact during optimization. The optimized result shows that the best dr and w are 523 nm and 1.488 μm, respectively. The simulated electric field distributions of the PD with the best parameters are shown in Fig. 2.

As shown in Figs. 2(e)–2(h), input light propagates along the edge of the Ge mesa, while in the center of the circle, the field distribution is weak. Thus, if the metal contact is placed in the center of the Ge circle, the absorption of metal will be minimum.
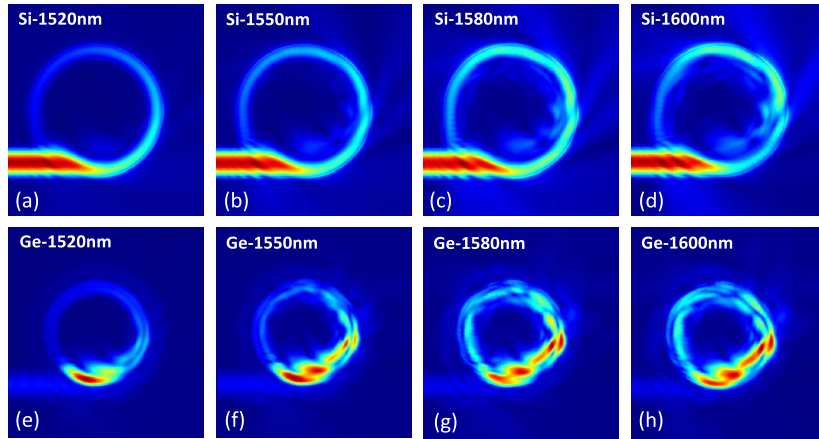

Fig. 1. Schematic of the light-trapping-structure Ge PD: (a) 3D view, (b) top view, and (c) side view along the incident direction; (b) and (c) hide all metal layers. Doping is not shown.

Fig. 2. Field distributions at different wavelengths in the proposed PD. (a)–(d) Distributions in silicon layer and (e)–(h) distributions in germanium layer.

Then, we add the metal contact in the model and simulate the responsivity again with the optimized parameters. We detect the electric field distribution in the Ge mesa with a 3D monitor, and then calculate the absorbance of Ge using the detected field distribution. According to Eq. (1), we can calculate the responsivity R of the PD:

$$R = \frac{I_{\text{ph}}}{P_{\text{in}}} = \alpha\eta_i \frac{e}{hf}, \tag{1}$$

where I_{ph} is photocurrent, P_{in} is input optical power, α is calculated optical absorbance of the Ge, η_i is internal quantum efficiency (η_i is set to one in the following simulation), e is elementary charge, h is the Planck constant, and f is the frequency of input light. The total external quantum efficiency can be defined as $\alpha\eta_i$. The calculated responsivity is shown in Fig. 3. To demonstrate the influence of metal absorption, we simulate the responsivity with and without a metal contact. As shown in Fig. 3, the responsivity with metal contact is up to 0.98 A/W at 1600 nm. The simulation results also show that the metal absorption at longer wavelengths is stronger than that at shorter wavelengths. The main reason can be found in Fig. 2. As shown in Figs. 2(e)–2(h), the field distribution is different at different wavelengths. Compared with shorter wavelengths, the mode size at longer wavelengths is larger,

and occupies more space in the Ge mesa. Thus, the field distribution at longer wavelengths is closer to the center of the circle, which leads to larger metal absorption. Due to the weak absorption of Ge at longer wavelengths, optical beams will propagate longer path lengths before being completely absorbed. This will further increase the metal absorption at longer wavelengths.

The simulated responsivity shows ripples especially at longer wavelengths. Ripples come from the resonance in the Ge mesa. Because the absorption of Ge decreases as wavelength increases, the resonance becomes stronger at longer wavelengths, which induces stronger ripples at longer wavelengths.

3. EXPERIMENTAL RESULTS

The PD is fabricated by a commercial SiP platform. Figure 4 shows an optical micrograph of the fabricated PD. Received optical signal is coupled into the PD chip by a grating coupler (GC). A linear taper used as a spot size converter connects the single mode waveguide and the input waveguide of the PD. The PD has three electrical pads arranged as ground-signal-ground (GSG) mode. The performance of the PD is tested by static measurement, small-signal RF measurement, and optical signal transmission measurement.
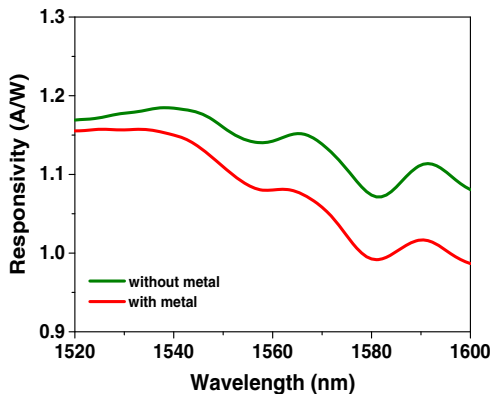
Fig. 3. Calculated responsivity of the circular Ge PD.
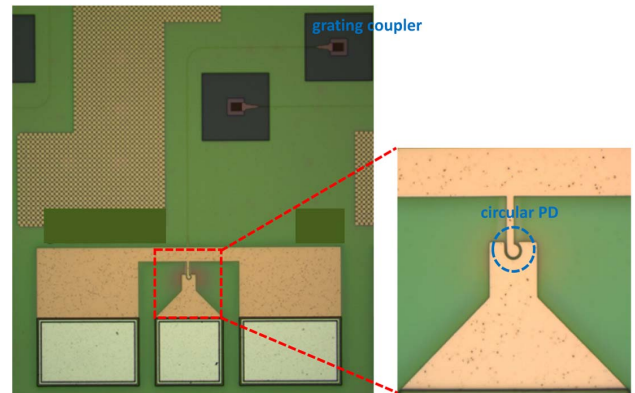
Fig. 4. Optical micrograph of the fabricated circular Ge PD.
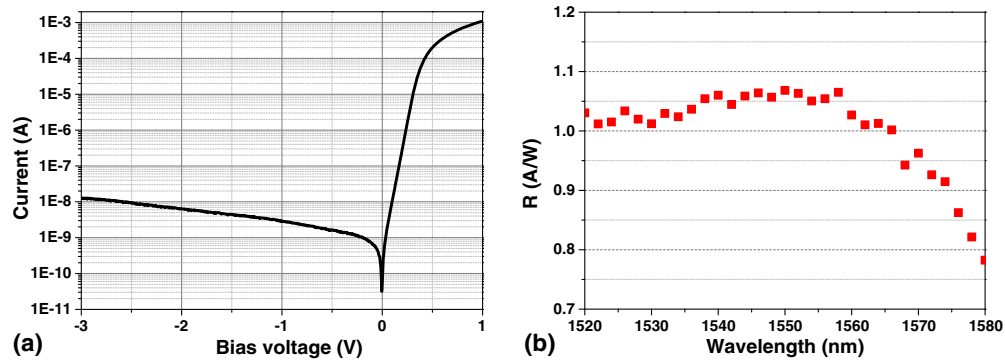
**Fig. 5.**   (a) Dark current versus voltage and (b) normalized responsivity at different wavelengths.

A. Static Measurement

Static measurements include dark current and responsivity measurements. We used a Santec tunable laser as the light source, and a Kethiley source meter to supply the bias voltage. The light source was turned off when measuring the dark current, and turned on when measuring the responsivity. The measured dark current versus bias voltage (*I-V*) and the normalized responsivity are shown in Fig. 5.

In Fig. 5(a), the proposed PD shows low dark currents, which is about 2.9 and 6.4 nA at −1 and −2 V bias, respectively. A low dark current indicates the high quality of epitaxial Ge. To get the net responsivity of the PD, the coupling loss of the GC should be normalized. We put a test structure of the GC near the PD to measure coupling loss, which is about −4.5 dB/facet at the central wavelength of the GC. Since coupling loss is high when the wavelength is over 1580 nm, we measured the responsivity in the range of 1520–1580 nm, which covers whole C-band. Figure 5(b) shows the normalized responsivity at different wavelengths. The responsivity is around 1.05 A/W at wavelengths between 1520 and 1560 nm, and descends at wavelengths beyond 1560 nm. At 1580 nm, the responsivity drops to 0.78 A/W. Compared with Fig. 3, it can be seen that the measured result is lower than the simulated one, especially at longer wavelengths. The difference mainly comes from two kinds of loss that could not be modeled in simulation. The first one is scattering loss induced by a facet sidewall of selectively grown Ge mesa. Scattering loss is more serious at longer wavelengths due to the weaker absorption and longer light path length. The second one is doping absorption loss in Si and Ge.

B. Small-Signal RF Measurement

The OE bandwidth of the proposed circular Ge PD is obtained by small-signal RF measurement. A 67 GHz Keysight light wave component analyzer (LCA) is employed with a built-in laser and modulator. A 67 GHz GSG probe is used to connect the pad of the PD. The reverse bias voltage is supplied by a Keithley source meter through a bias tee. Optical signal generated from the LCA is detected by the PD, and the converted RF signal is output through the bias tee. In the measurement, the bandwidth influence from RF cables and probes is calibrated. The normalized frequency responses with different bias voltage are shown in Fig. 6. At 0 V, the 3 dB bandwidth is about 26 GHz. With bias voltage increasing, the 3 dB
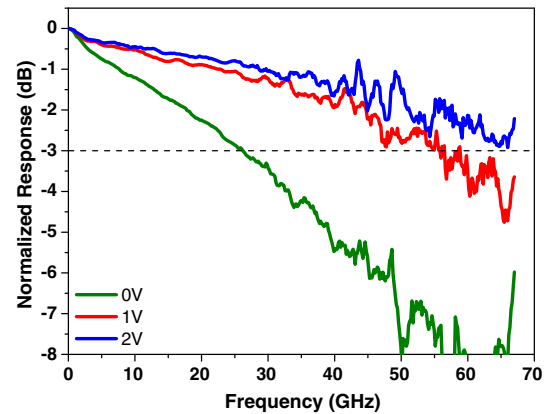
Fig. 6.   Normalized frequency response of the proposed Ge PD.

bandwidth increases rapidly, and can reach 55 and 67 GHz at −1 and −2 V bias, respectively.

There are two major factors that can affect the OE bandwidth of the typical PIN PD: the transit time of carriers and capacitance–resistance (RC) constant. The 3 dB bandwidth can be calculated by

$$f_{3\,dB} = \frac{1}{\sqrt{f_{tr}^{-2} + f_{RC}^{-2}}}, \qquad (2)$$

where f_{tr} is carrier transit frequency, and f_{RC} is the RC bandwidth. The thickness of Ge in our PD is 500 nm (including doping depth). If the carriers move at saturation drift velocity, the estimated f_{tr} is about 90 GHz [11]. f_{RC} is defined as

$$f_{RC} = \frac{1}{2\pi RC}, \qquad (3)$$

where C is the junction capacitance of the PD, which is proportional to the area of Ge. According to Eq. (3), f_{RC} could be improved by reducing the area of Ge.

For our light-trapping Ge PD, the photon lifetime may also affect the bandwidth. As shown in Fig. 2, received light propagates along the edge of the circular absorption area. Because the absorption coefficient at longer wavelengths is weak, the light circulates several times until it is completely absorbed. A long propagation time means a long photon lifetime. However, for the 3 μm radius circle, even if the light propagates 10 circles,

the propagation time is about 2.5 ps (group index of Ge is assumed to be four), which corresponds to a 400 GHz bandwidth, much larger than the measured 67 GHz bandwidth. Thus, the influence of propagation time can be neglected.

According to the above analyses, we can qualitatively explain the bandwidth variation of the proposed PD at different voltages. At 0 V, due to the weak electric field in Ge, the velocities of carriers are low and f_{tr} is small. However, owing to the small size of the proposed circular PD, f_{RC} can still guarantee a 26 GHz bandwidth. With increasing bias voltage, the drift velocities of carriers increase, and the junction capacitance reduces due to the increasing depletion region width. f_{tr} and f_{RC} both increase, and f_{RC} becomes the limitation of bandwidth at high voltages. Compared with our vertical rectangular PD with a Ge area of 4×20 μm^2, which is fabricated by the same process and has a 3 dB bandwidth of 35 GHz at –3 V bias, the 67 GHz bandwidth of the proposed PD benefits from the compressed area of Ge.

Table 1 gives a performance comparison of bandwidth, responsivity, and dark current between our PD and other works. Benefiting from the light-trapping circle and compressed absorption area, the proposed PD can relax the trade-off between bandwidth and responsivity to a certain extent.

C. High-Speed Transmission Measurement

The performance of the proposed PD in a high-speed optical transmission system is verified by measuring the BER and eye diagram of PAM-4 signal. The experiment setup is shown in Fig. 7(a). In our experiment, various baud rates of PAM-4 signal are generated by an arbitrary waveform generator (AWG) whose sampling rate is 120 GS/s (Keysight M8194A). The output amplitude of AWG is $0.5V_{pp}$. A 67 GHz commercial driver is used to amplify the output of the AWG and then connected to a commercial intensity Mach–Zehnder modulator (MZM). The 3 dB bandwidth of MZM is 40 GHz. A tunable laser is used as the light source with a wavelength of 1550 nm and output power of 15 dBm. On the receiver side, the optical

signal is amplified by an erbium doped fiber amplifier (EDFA) and then detected by our light-trapping PD. A 67 GHz GSG RF probe and bias tee are also used, as mentioned in Subsection 3.B. Since we could not find a high-bandwidth trans-impedance amplifier (TIA), we used the EDFA to increase the amplitude of the detected signal, which is necessary for signal capturing in a real-time oscilloscope. The sampling rate of the real-time oscilloscope (Keysight UXR0704A) is 256 Gs/s. The output signal of the PD can also be captured by sampling the oscilloscope for eye diagram measurement.

In our experiment, offline DSP is utilized on both Tx and Rx sides to jointly optimize the performance of the transmission system. In Tx DSP, a pseudo random bit sequence (PRBS) PAM-4 signal is generated with a word length of 2^{15}. Then non-linearity of the MZM and driver is compensated for simultaneously. A root raised cosine (RRC) filter and pre-emphasis are employed to eliminate the bandwidth limitation of the MZM and end-to-end transmission system. On the Rx side, the received data are first re-sampled and synchronized. Then a 51-tap adaptive feed forward equalizer (FFE) is utilized to compensate for the linear impairment generated in high-speed transmission. A Volterra equalizer is used to compensate for the nonlinear impairment, and an adaptive maximum likelihood sequence estimation (MLSE) equalizer with memory length of 3 bits is used to compensate for the residual inter-symbol interference (ISI). Finally, BER is calculated by comparing the demodulated data with transmitted data generated on the Tx side.

Figure 7(b) shows a BTB eye diagram of the PAM-4 signal with different baud rates. In the measurement, a $\sin(x)/x$ function built in the oscilloscope (Keysight N1000A DCA-X) is used. It can be seen that the clear eye diagram of the 100 GBaud PAM-4 signal is measured.

The transmission BERs of the PAM-4 signal with different bit rates and transmission distances are measured and demonstrated in Fig. 8(a). The highest bit rate for BTB is 240 Gb/s with a BER of 1.6×10^{-2}, which is lower than the SD-FEC threshold, i.e., 2×10^{-2}. We think the highest bit rate is limited

Table 1. Performance Comparison between Proposed PD and Other Works

Reference	Structure of Ge	3 dB Bandwidth (GHz)	Responsivity (A/W)	Dark Current (nA)	Dark Current Density (mA/cm²)
[9]	Rectangle (0.1×10 μm^2)	265 at 2 V	0.3 at 1550 nm	≤200 at 2 V	≤5000[a]
[10]	Rectangle (0.5×14.2 μm^2)	67 at 1 V	0.74 at 1550 nm ~0.52 at 1570 nm	3.6 at 2 V	~158[a]
[24]	Rectangle	67 at 2 V	0.9 at 1550 nm	–	90 at 1 V
[25]	Rectangle (3×15 μm^2)	42 at 4 V	1 at 1550 nm ~0.58 at 1580 nm (with edge coupler)	18 at 1 V	60
[26]	Rectangle (7.4×50 μm^2)	31 at 2 V	0.89 at 1550 nm ~0.82 at 1580 nm	169 at 2 V	51
[29]	Rectangle (1.5×12 μm^2)	40 at 1 V	0.7 at 1550 nm ~0.5 at 1580 nm	1.16 at 1 V	~6[a]
[30]	Rectangle (1.3×4 μm^2)	45 at 1 V	0.8 at 1500 nm (TM mode)	3 at 1 V	~57[a]
Our previous work	Rectangle (4×20 μm^2)	35 at 3 V	0.85 at 1550 nm	20 at 2 V	25
This work	Circular ($9 \times \pi$ μm^2)	67 at 2 V	1.05 at 1550 nm 0.78 at 1580 nm	6.4 at 2 V	23

[a]Data calculated using the referenced paper.
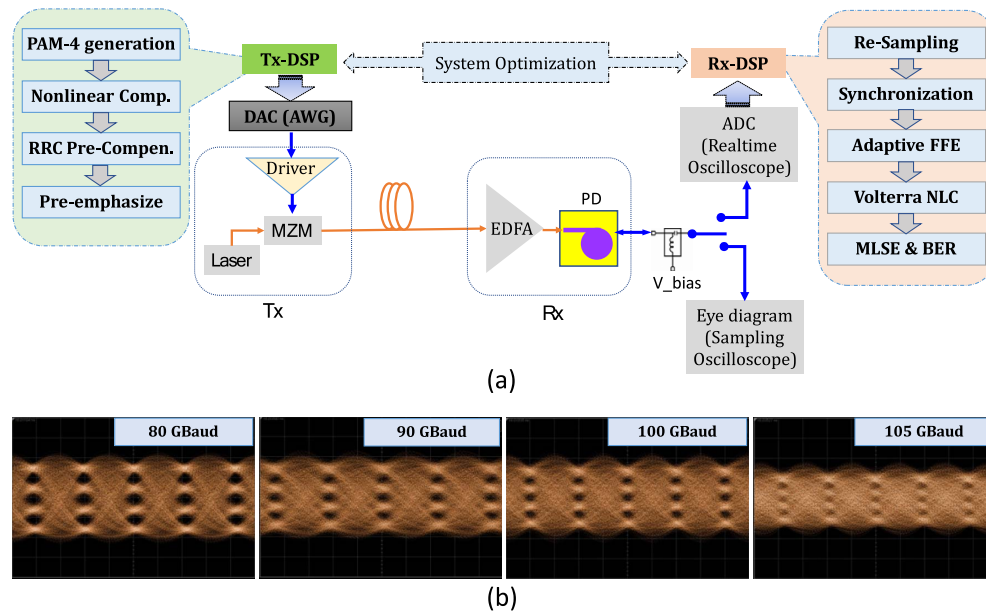
Fig. 7.   (a) Experiment setup of high-speed PAM-4 signal transmission system and (b) BTB eye diagram of 80, 90, 100, and 105 GBaud PAM-4 signals.
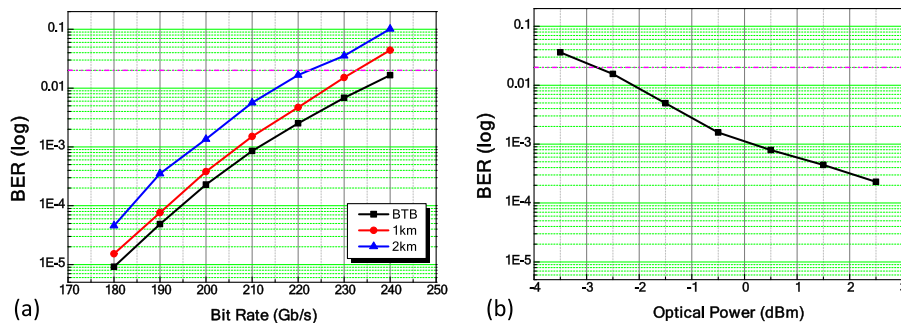
Fig. 8.   (a) BER versus different bit rates with BTB, 1 km, and 2 km transmissions; (b) BTB BER of 200 Gb/s PAM-4 versus different optical power.

by the bandwidth of the MZM and sampling rate of the AWG, i.e., 120 GS/s. Since the proposed PD is designed to work in the C-band, CD would affect the BER performance in such a high-speed transmission system. With 1 km standard single mode fiber (SSMF) transmission, the BER of the 240 Gb/s PAM-4 signal is 4.4×10^{-2}, and the highest bit rate below the SD-FEC threshold is decreased to 230 Gb/s. When the SSMF length is 2 km, the highest bit rate is further decreased to 220 Gb/s.

To analyze the receiver sensitivity of 100 GBaud/s PAM-4 signal transmission, we tested the BTB BER with various received optical powers. The result is shown in Fig. 8(b). We also used the SD-FEC threshold as the criteria, and the receiver sensitivity was −2.5 dBm with 200 Gb/s PAM-4 signal transmission.

4. CONCLUSION

We proposed and demonstrated a novel light-trapping-structure vertical Ge PD. In our scheme, circular Ge with

3 μm radius is designed to constrain the optical signal in the absorption area. Benefiting from the light-trapping circle, the trade-off between bandwidth and responsivity can be relaxed. With −2 V bias voltage, the measured 3 dB bandwidth is around 67 GHz, and responsivity is around 1.05 A/W at wavelengths between 1520 and 1560 nm. At 1580 nm, the responsivity is still over 0.78 A/W. Measured results show that high OE bandwidth and high responsivity are achieved simultaneously. In addition, the proposed PD also shows good performance of the dark current, which is only about 6.4 nA at −2 V bias. High-speed optical transmission based on the proposed PD is experimentally demonstrated with offline DSP; 240 Gb/s PAM-4 signal transmission is achieved, and the BTB BER is 1.6×10^{-2}. After 1 and 2 km SSMF transmission, the measured highest data rates below SD-FEC are 230 and 220 Gb/s, respectively. For the 100 GBaud PAM-4 signal, a clear eye diagram is obtained, and −2.5 dBm receiver sensitivity is measured in BTB transmission.

†These authors contributed equally to this paper.

REFERENCES

1. R. Soref, "The past, present, and future of silicon photonics," IEEE J. Sel. Top. Quantum Electron. **12**, 1678–1687 (2006).
2. N. Izhaky, M. T. Morse, S. Koehl, O. Cohen, D. Rubin, A. Barkai, G. Sarid, R. Cohen, and M. J. Paniccia, "Development of CMOS-compatible integrated silicon photonics devices," IEEE J. Sel. Top. Quantum Electron. **12**, 1688–1698 (2006).
3. X. Chen, M. M. Milosevic, S. Stanković, S. Reynolds, T. D. Bucio, K. Li, D. J. Thomson, F. Gardes, and G. T. Reed, "The emergence of silicon photonics as a flexible technology platform," Proc. IEEE **106**, 2101–2116 (2018).
4. A. Y. Piggott, J. Lu, K. G. Lagoudakis, J. Petykiewicz, T. M. Babinec, and J. Vučković, "Inverse design and demonstration of a compact and broadband on-chip wavelength demultiplexer," Nat. Photonics **9**, 374–377 (2015).
5. B. Shen, P. Wang, R. Polson, and R. Menon, "An integratednanophotonics polarization beamsplitter with 2.4 × 2.4 μm² footprint," Nat. Photonics **9**, 378–382 (2015).
6. M. Li, L. Wang, X. Li, X. Xiao, and S. Yu, "Silicon intensity Mach–Zehnder modulator for single lane 100 Gb/s applications," Photon. Res. **6**, 109–116 (2018).
7. M. Sakib, P. Liao, C. Ma, R. Kumar, D. Huang, G.-L. Su, X. Wu, S. Fathololoumi, and H. Rong, "A high-speed micro-ring modulator for next generation energy-efficient optical networks beyond 100 Gbaud," in *Conference on Lasers and Electro-Optics* (2021), paper SF1C.3.
8. Y. Zhang, H. Zhang, M. Li, P. Feng, L. Wang, X. Xiao, and S. Yu, "200 Gbit/s optical PAM4 modulation based on silicon microring modulator," in *European Conference on Optical Communication* (2020), paper Th3A-1.
9. S. Lischke, A. Peczek, J. S. Morgan, K. Sun, D. Steckler, Y. Yamamoto, F. Korndörfer, C. Mai, S. Marschmeyer, M. Fraschke, A. Krüger, A. Beling, and L. Zimmermann, "Ultra-fast germanium photodiode with 3-dB bandwidth of 265 GHz," Nat. Photonics **15**, 925–931 (2021).
10. H. Chen, P. Verheyen, P. De Heyn, G. Lepage, J. De Coster, S. Balakrishnan, P. Absil, W. Yao, L. Shen, G. Roelkens, and J. Van Campenhout, "–1 V bias 67 GHz bandwidth Si-contacted germanium waveguide p-i-n photodetector for optical links at 56 Gbps and beyond," Opt. Express **24**, 4622–4631 (2016).
11. X. Hu, D. Wu, H. Zhang, W. Li, D. Chen, L. Wang, X. Xiao, and S. Yu, "High-speed and high-power germanium photodetector with a lateral silicon nitride waveguide," Photon. Res. **9**, 749–756 (2021).
12. Y. Ishikawa and K. Wada, "Germanium for silicon photonics," Thin Solid Films **518**, S83–S87 (2010).
13. J. Wang and S. Lee, "Ge-photodetectors for Si-based optoelectronic integration," Sensors **11**, 696–718 (2011).
14. W. N. Ye and Y. Xiong, "Review of silicon photonics: history and recent advances," J. Mod. Opt. **60**, 1299–1320 (2013).
15. G. Dehlinger, S. J. Koester, J. D. Schaub, J. O. Chu, Q. C. Ouyang, and A. Grill, "High-speed germanium-on-SOI lateral PIN photodiodes," IEEE Photon. Technol. Lett. **16**, 2547–2549 (2004).
16. J. Kang, S. Takagi, and M. Takenaka, "Ge photodetector monolithically integrated with amorphous Si waveguide on wafer bonded Ge-on-insulator substrate," Opt. Express **26**, 30546–30555 (2018).
17. D. Benedikovic, L. Virot, G. Aubin, J. M. Hartmann, F. Amar, X. Le Roux, C. Alonso-Ramos, E. Cassan, D. Marris-Morini, P. Crozat, F. Boeuf, J. M. Fedeli, C. Kopp, B. Szelag, and L. Vivien, "40 Gbps heterostructure germanium avalanche photo receiver on a silicon chip," Optica **7**, 775–783 (2020).
18. D. Benedikovic, L. Virot, G. Aubin, F. Amar, B. Szelag, B. Karakus, J.-M. Hartmann, C. Alonso-Ramos, X. Le Roux, P. Crozat, E. Cassan, D. Marris-Morini, C. Baudot, F. Boeuf, J.-M. Fédéli, C. Kopp, and L. Vivien, "25 Gbps low-voltage hetero-structured silicon-germanium waveguide pin photodetectors for monolithic on-chip nanophotonic architectures," Photon. Res. **7**, 437–444 (2019).
19. L. Virot, D. Benedikovic, B. Szelag, C. Alonso-Ramos, B. Karakus, J.-M. Hartmann, X. Le Roux, P. Crozat, E. Cassan, D. MarrisMorini, Ch. Baudot, F. Boeuf, J.-M. Fédéli, C. Kopp, and L. Vivien, "Integrated waveguide PIN photodiodes exploiting lateral Si/Ge/Si heterojunction," Opt. Express **25**, 19487–19496 (2017).
20. X. Hu, D. Wu, H. Zhang, W. Li, D. Chen, L. Wang, X. Xiao, and S. Yu, "High-speed lateral PIN germanium photodetector with 4-directional light input," Opt. Express **28**, 38343–38354 (2020).
21. K.-W. Ang, T.-Y. Liow, M.-B. Yu, Q. Fang, J. Song, G.-Q. Lo, and D.-L. Kwong, "Low thermal budget monolithic integration of evanescent-coupled Ge-on-SOI photodetector on Si CMOS platform," IEEE J. Sel. Top. Quantum Electron. **16**, 106–113 (2010).
22. T.-Y. Liow, K.-W. Ang, Q. Fang, J.-F. Song, Y.-Z. Xiong, M.-B. Yu, G.-Q. Lo, and D.-L. Kwong, "Silicon modulators and germanium photodetectors on SOI: monolithic integration, compatibility, and performance optimization," IEEE J. Sel. Top. Quantum Electron. **16**, 307–315 (2010).
23. F. Boeuf, A. Fincato, L. Maggi, J. F. Carpentier, P. Le Maitre, M. Shaw, S. Cremer, N. Vulliet, C. Baudot, S. Monfray, S. Jan, C. Deglise, J. R. Manouvrier, C. Durand, A. Simbula, D. Goguet, P. Bar, D. Ristoiu, F. Leverd, L. Babaud, A. Daverio, M. Binda, A. Bazzotti, A. Canciamilla, L. Ramini, M. Traldi, and P. Gambini, "A silicon photonics technology for 400-Gbit/s applications," in *IEEE International Electron Devices Meeting (IEDM)* (2020), pp. 33.1.1–33.1.4.
24. D. Zhu, J. Zheng, Y. Qamar, O. Martynov, F. Rezaie, and E. Preisler, "A high performance Ge PIN photodiode compatible with high volume silicon photonics production processes," in *IEEE 15th International Conference on Group IV Photonics (GFP)* (2018), pp. 1–2.
25. L. Vivien, J. Osmond, J.-M. Fédéli, D. Marris-Morini, P. Crozat, J.-F. Damlencourt, E. Cassan, Y. Lecunff, and S. Laval, "42 GHz p.i.n germanium photodetector integrated in a silicon-on-insulator waveguide," Opt. Express **17**, 6252–6257 (2009).
26. T. Yin, R. Cohen, M. M. Morse, G. Sarid, Y. Chetrit, D. Rubin, and M. J. Paniccia, "31 GHz Ge n-i-p waveguide photodetectors on silicon-on-insulator substrate," Opt. Express **15**, 13965–13971 (2007).
27. M. M. P. Fard, G. Cowan, and O. Liboiron-Ladouceur, "Responsivity optimization of a high-speed germanium-on-silicon photodetector," Opt. Express **24**, 27738–27752 (2016).
28. D. Ahn, C. Hong, J. Liu, W. Giziewicz, M. Beals, L. C. Kimerling, and J. Michel, "High performance, waveguide integrated Ge photodetectors," Opt. Express **15**, 3916–3921 (2007).
29. M. J. Byrd, E. Timurdogan, Z. Su, C. V. Poulton, N. M. Fahrenkopf, G. Leake, D. D. Coolbaugh, and M. R. Watts, "Mode-evolution-based coupler for high saturation power Ge-on-Si photodetectors," Opt. Lett. **42**, 851–854 (2017).
30. C. T. DeRose, D. C. Trotter, W. A. Zortman, A. L. Starbuck, M. Fisher, M. R. Watts, and P. S. Davids, "Ultra compact 45 GHz CMOS compatible germanium waveguide photodiode with low dark current," Opt. Express **19**, 24897–24904 (2011).
31. J. Cui and Z. Zhou, "High-performance Ge-on-Si photodetector with optimized DBR location," Opt. Lett. **42**, 5141–5144 (2017).
32. C. Lin, D. Huang, T. Shih, H. Kuo, and S. Chang, "Increasing responsivity-bandwidth margin of germanium waveguide photodetector with simple corner reflector," Opt. Express **29**, 10364–10373 (2021).
33. M. Rouvière, M. Halbwax, J.-L. Cercus, E. Cassan, L. Vivien, D. Pascal, M. Heitzmann, J.-M. Hartmann, and S. Laval, "Integration of germanium waveguide photodetectors for intrachip optical interconnects," Opt. Eng. **44**, 75402–75406 (2005).
34. L. M. Nguyen, R. Kuroyanagi, T. Tsuchizawa, Y. Ishikawa, K. Yamada, and K. Wada, "Stress tuning of the fundamental absorption edge of pure germanium waveguides," Opt. Express **23**, 18487–18492 (2015).